Research Square

Preprints are preliminary reports that have not undergone peer review.
They should not be considered conclusive, used to inform clinical practice,
or referenced by the media as validated information.

Abnormal cerebellar development is involved in dystonia-like behaviors and motor dysfunction of autistic BTBR mice

Rui Xiao
Army Medical University https://orcid.org/0000-0001-9442-6464
Hongyu Zhong
Army Medical University
Xin Li
Army Medical University
Yuanyuan Ma
Army Medical University
Ruiyu Zhang
Army Medical University
Lian Wang
Army Medical University
Zhenle Zang
Army Medical University
Xiaotang Fan (fanxiaotang2005@163.com)
https://orcid.org/0000-0001-5694-1828

Research

Keywords: Autism spectrum disorders, Dystonia, Movement disorder, Cerebella, Neurodevelopment

Posted Date: December 23rd, 2019

DOI: https://doi.org/10.21203/rs.2.19516/v1

License: This work is licensed under a Creative Commons Attribution 4.0 International License.
Read Full License

Abstract

Background: Motor control and learning impairments are common complications in autistic individuals. Abnormal cerebellar development during critical phases may disrupt these motor functions and lead to the development of autistic motor dysfunction. However, the underlying mechanisms behind these impairments are not clear.

Methods: Dystonic behavior was elicited using tail suspension. Motor control and learning were detected by means of the grid hang test, ladder rung walking, accelerating rotarod, and open field locomotion. Cerebellar development was morphometrically and histologically detected during critical phases. RNA sequencing was used to compare differential gene expression to provide an in-depth interpretation of molecular mechanisms.

Results: BTBR mice, as a model of autism, exhibited severe dystonic behavior and motor coordination or motor learning impairments. The onset of these abnormal movements coincided with the increased proliferation of granule neurons and enhanced foliation, and Purkinje cells exhibited morphological hypotrophy with increased dendritic spine formation but suppressed maturation. The migration of granule neurons seemed unaffected. Transcriptional analyses confirmed the differential expression of genes involved in abnormal neurogenesis and revealed *TRPC6* as a critical regulator in proliferation and synaptic formation.

Conclusion: These findings indicate that abnormal cerebellar development is closely related to dystonia and motor dysfunction of BTBR mice and that *TRPC6* may be a novel risk gene for ASD that may participate in the pathological process of autistic movement disorders.

Background

Autism spectrum disorder (ASD) is a pervasive neurodevelopmental disorder that is characterized by persistent defects in social communication and interaction and restricted, repetitive, inflexible behaviors and interests (1). It is commonly diagnosed in early childhood, and the prevalence of ASD has increased dramatically throughout the last decades (2). The interaction of genetic and environmental factors was recently hypothesized to contribute to the pathogenesis of ASD (3, 4), but the etiology of the disorder remains far from clear.

In addition to the core symptoms, autistic subjects frequently present with complex motor impairments, such as ataxia, dystonia, and akinesia (5). Notably, a systematic research on the prevalence of movement disorders in ASD associated with specific genetic syndromes revealed 43.6–100% for ataxia and 25.0-48.3% for tremor, with additional reports for dystonia and rigidity (6). Several clinicians have proposed that these atypical movement impairments are a predictor for ASD because these impairments often appear prior to the classical behaviors of ASD (7, 8). Motor disturbances may underlie some of the behavioral core features in autism. The contribution of movements to social cognition and cascade effects on social communication in individuals with autism have been reported (5, 9). Notably,

therapeutic medicines for motor dysfunction, such as hyperactivity, have improved social interaction deficits and recognition memory impairment in ASD subjects (10). It is quite essential and meaningful to illuminate the relationship between autism and motor dysfunctions to provide comprehensive and precise treatment. Several hypotheses have been raised, but more evidence is needed, and the shared underlying mechanisms with autism should be further examined.

Several brain regions have been implicated in the pathogenesis of ASD, but cerebellar abnormalities are the most reproducibly studied alterations in this disorder. Neuropathological studies showed lower Purkinje cell counts, missed or ectopic neurons of deeper cerebellar nuclei (DCN), cortical thickness alterations, foliation dysplasia and migration impairments in the cerebellar cortex of individuals with ASD (11–14). Indeed, cerebellar lesions are associated with increased rates of autistic behavior, and recent evidence has suggested suppressed social function, restrictive or repetitive behaviors, and motor impairment symptoms such as ataxia, dystonia and tremor (15). It was recently proposed that early perinatal alterations of the cerebellum are involved in ASD pathogenesis, which is supported by the finding that autism genes are frequently coexpressed with aberrant cerebellar development (16).

The cerebellum is a typically well-defined lamellar structure that consists of the molecular layer (ML), Purkinje cell layer (PCL) and inner granule layer (IGL) (17). During cerebellum development, billions of granule neurons proliferate in the external granule layer (EGL) and then descend and migrate to destinations in the IGL, leaving “T-shaped” parallel fibers that are arranged in parallel along the cerebellar folia axis and synapse on the dendritic arbors of Purkinje cells (PCs) (18, 19). The PC axons further travel to the DCN and project more broadly. As the sole efferent neurons in the cerebellum, Purkinje neurons regulate all of the information transfer and are responsible for cerebellar function (20). Notably, the loss of cerebellar Purkinje cells is one of the most consistent findings in postmortem studies in patients with ASD (21). Therefore, a follow-up question is to what extent developmental morphological aberrations of the cerebellum concomitantly occur in specific motor impairment.

We investigated the contribution of abnormal cerebellar development to movement disorders in a mouse model of idiopathic ASD, the BTBR T^{+} $Itpr3^{tf}$/J (BTBR) inbred strain, compared to the control wild-type (WT) C57BL/6J strain. BTBR mice are a robust behavioral phenotype that model core autism-like impairments and exhibit striking anatomical features in the cerebellum. The present study revealed distinct dystonic behaviors and motor learning impairments in BTBR mice that began in early postnatal days. Concomitant with the progression of behavioral impairment, a hyperplastic cerebellum with enhanced foliation was identified due to the abnormally increased proliferation of granule cell precursors (GCPs). Moreover, Purkinje neurons were morphologically altered in the cerebella of BTBR mice and exhibited hypotrophy and disturbed spine formation. Evidence from RNA sequencing indicated a considerable negative regulation of nervous system development, and transient receptor potential canonical channel (TRPC) family, including TRPC6 as the core and TRPC3, TRPC4, played key roles in the signal regulation of the inaccurate development. Together, these findings suggest that abnormal cerebellar development, which may be regulated by TRPC, was involved in the pathological progression from movement disorders to autism.

Materials And Methods

Animals

BTBR mice were originally obtained from Jackson Laboratory (BTBR *T*$^{+}$*Itpr3*^{tf}/J; stock number 002282) and maintained in our mouse colony at the Army Medical University. Wild-type C57BL/6J mice were used as controls and were provided by the Army Medical University. Only male mice were used in the experiments. After weaning at 3 weeks, mice were group-housed with 4-6 mice per cage under a controlled environment (22±2°C, 45±10% humidity, 12 h light/dark cycle) with free access to water and food. The Army Medical University approved all experiments, which were performed according to the accepted standards of animal care. Efforts were made to reduce animal suffering.

Behavioral assays

Mice were examined periodically using the tail suspension test and grid hang test from early postnatal days to 5 months. Other behavioral assessments, such as horizontal ladder rung walking, rotarod and open field, were initiated at 8 weeks.

Tail suspension test

Mice were suspended by their tails for 60 s. The activity of the mice was recorded by a camera to observe the presence of dystonia-like behavior, as references described (22, 23), including hyperflexion, trunk twisting, hyperextension, and forelimb or hindlimbs clasping. These phenotypes were recorded from postnatal (P) day 3 to day 150.

Grid hang test

Motor coordination and strength were detected by putting the mice on a 30×50 cm wire grid with 0.5 cm^2 openings. The grid was inverted after the mouse grabbed the grid with its fore- and hindlimbs, and the latency to fall off was recorded. Movement on the grid and the paw placement of the mice were observed during the test.

Horizontal ladder rung walking test

Skilled fore- and hindlimb coordination and fine motor function were assessed by the horizontal ladder rung walking test (24). To subtly test coordination, the difficulty of the task was divided into two patterns: pattern A used a regular rung arrangement with 2 cm intervals, and pattern B used an irregular rung pattern with randomly spaced rungs at intervals from 1-3 cm. Mice were put on one side of the ladder (30 cm above the ground) and free to cross it. The whole crossing process was filmed with a high-definition video camcorder (Logitech C930e), and behaviors were analyzed. The total limb falls and time to cross the ladder were recorded to assess motor function. Five trials were performed on each mouse, and the average value was calculated.

Accelerating rotarod test

Motor coordination and motor learning were detected using the accelerating rotarod test. Mice were put on an accelerating rod (3 cm diameter, 14 cm above the pedestal), and the speed was set to 5 rpm with a uniform acceleration to 40 rpm in 5 min. The latency of mouse falling from the rotating rod was calculated. Five trials were performed on each mouse per day for 5 consecutive days to assess motor learning in each group.

Open field locomotion test

Mice were put in an open field to assess locomotor activity. The apparatus was a square plexiglass cage (40×40×30 cm) illuminated at ~200 lux. As previously described (25), square grid lines were predefined by a computer that divided the open field chamber into a central zone and periphery. Mice were placed in the center of the apparatus, and locomotion was traced for 30 min using Ethovision 11.0 software (Noldus). The total distance in all zones and the center zone were calculated to assess the activity of mice. The apparatus was cleaned with 70% ethanol between trials.

Histology and immunohistochemistry

Adult mice were completely anesthetized with sodium pentobarbital and transcardially perfused with ice-cold 0.01 M phosphate-buffered saline (PBS) followed by 4% paraformaldehyde (PFA) in PBS. Neonatal mice received BrdU injection (50mg/kg i.p.) and then were decapitated 2 hours later, and the needed tissues were dissected. Dissected cerebella were postfixed in 4% PFA for 48 h and dehydrated in a 50-100% gradient alcohol series. Tissues were soaked twice in trichloromethane for 20 min and covered twice with melted paraffin for 30 min. Cerebella were paraffin-embedded, and then sagittal sections (5 μm) were collected. All sections used in each mouse were taken from the same medial lateral position on the cerebellum to allow comparisons. Paraffin sections were performed dewaxing and antigen retrieval before used. For hematoxylin-eosin (HE) staining, sections were incubated in hematoxylin (ZLI-9610, ZSJQ-Bio, China) for 10 min, washed in flowing water, differentiated by 75% hydrochloric acid in alcohol for 1 min, washed in flowing water when the nucleus was black to blue, incubated in eosin (ZLI-9612, ZSJQ-Bio, China) for 10 s, dehydrated in 95% alcohol for 1 min, and mounted in DPX (06522, Sigma, USA). For immunohistochemical staining, sections were processed by washing in 0.3% Triton-X/PBS, blocking in 3% bovine serum albumin (BSA) (37°C, 2h), and incubation with the following primary antibodies (room temperature (RT), overnight): (1) mouse anti-5-bromo-2'-deoxyuridine (BrdU) (1:500, BD PharmingenTM, USA); (2) rabbit anti-Ki67 (1:1000, Thermo, USA); (3) rabbit anti-neuronal nuclei (NeuN) (1:200, Abcam, USA); rabbit anti-s100b (1:500, CST, USA); rabbit anti-glial fibrillary acidic protein (GFAP) (1:500, Dako, Japan); and mouse anti-calbindin (CB) (1:1000, Swant, Switzerland). After washing in 0.01 M PBS for 30 min, sections were incubated with the corresponding secondary antibodies (RT, 3 h in darkness): Alexa Fluor 488-conjugated donkey anti-mouse IgG (1:500, Jackson Immunoresearch, USA); and cy3-conjugated donkey anti-rabbit IgG (1:500, Jackson Immunoresearch, USA). 4’,6-Diamidino-2-phenylindole (DAPI) (1:10000, Sigma-Aldrich, USA) was used to counterstain the nuclei in all sections. After air drying, sections were mounted with Vectashield (Vector Lab, USA). Sections for Nissl staining

were incubated in a cresyl violet solution containing acetic acid (C0117, ZSJQ-Bio, China) (37°C, 30 min), dehydrated in 95% alcohol for 1 min, and mounted in DPX (06522, Sigma, USA). The stained sections were observed under a Zeiss Axiovert microscope (Oberkochen, Germany) with a Zeiss Axiovision 4.0 system.

Golgi staining

Mice were decapitated immediately at postnatal day 14, and brains were dissected. Cerebella were rinsed and processed for Golgi staining with the FD Rapid Golgi Stain Kit (PK401A, FD Neurotechnologies, USA) according to the manufacturer's protocol. Sagittal sections (80 μm) were generated and mounted in DPX after drying. Slides were observed using a Zeiss Axiovert microscope. Sholl analysis was executed using the matched Zeiss Axiovision 4.0 system.

Western blot

Neonatal mice were decapitated, and their cerebella were dissected in ice-cold PBS. The total protein was extracted immediately, and protein concentrations were measured using a Bicinchoninic Acid Kit (Beyotime, China) as previously described (26). The total protein (20 μg) of each sample was separated by 10% SDS-polyacrylamide electrophoresis (80 V, 100 min) and then transferred to a polyvinylidene fluoride (PVDF) membrane (220 mA, 60 min). The membranes were washed in 1% Tween-20/Tris-buffered saline (TBS) (TBS-T), blocked in 5% BSA/TBS-T (RT, 2 h), and incubated with a primary antibodies (4°C, 12 h) (1) mouse anti-CB (1:2000, Swant, Switzerland) and (2) mouse anti-GAPDH (1:2000, Cell Cwbio, China), followed by peroxidase-conjugated goat anti-mouse secondary antibody IgG (1:1000, Santa Cruz Biotechnology, USA). Bands were visualized using the chemiluminescence detection kit (Pierce, USA) under a Gel-Pro analyzer (Bio-Rad Laboratories, USA). Band intensity was quantified in Image Lab (Bio-Rad Laboratories, USA), and calbindin protein was normalized to GAPDH.

Quantification

Comparable middle sagittal sections were selected for assessments. Cerebella sagittal area (mm^2) and perimeter (mm) were defined as shown in Fig.2E and calculated with a Zeiss Axiovision 4.0 system. Lobes separated clearly by fissures were calculated as the lobe number. Total BrdU- and Ki67-positive granule cell precursors were counted only in the EGL. BrdU-positive precursor density was calculated as all BrdU cells in the EGL / perimeter, and BrdU-positive cell proportion in the EGL was calculated as BrdU-positive cells /DAPI-stained nuclei in a high-power field of the EGL (218 μm length) in lobe IV/V. Bergmann soma in the PCL and fibers in the ML were counted under a 20X objective lens along the lobe axis (~450 μm length), and the densities were calculated. Purkinje neuron density and soma size were counted in each lobe along a 500 μm-length axis in the middle of each lobe. Among these cells, 10 Purkinje neurons were randomly selected, and their soma areas were measured by means of a Zeiss Axiovision 4.0 system.

For Golgi staining quantification, the outer terminals of the Purkinje dendritic branches were orderly linked, and the formative closed region was defined as the PC dendritic area. Primary dendrite length was measured as the primary dendrite of each Purkinje neuron from the soma up to the end at the surface of the ML. Sholl analysis was performed, as described previously (27). Purkinje neuron branches were incised by concentric circles with 5.5 μm radius steps from the soma, and intersections in each circle were counted. Dendrite spine density and classification were assessed referring to Risher (28). At least a 10 μm-length branch was calculated for the spine. Ten cells per mouse and 10 branches per cell were detected.

RNA-seq analyses

The whole cerebella of BTBR and WT mice were collected at postnatal day 14 for the mRNA sequencing assay. This experiment was performed by Novogene (Bejing, China). Libraries were generated using the NEBNext® Ultra™ RNA Library Prep Kit for Illumina® (NEB, USA) according to standard Illumina protocols. After clustering was performed in the cBot Cluster Generation System, the libraries were sequenced on an Illumina Hiseq platform with a 125 bp/150 bp paired-end reads strategy. The original image data were subjected to quality control, and reads containing adapter, poly-N reads and low-quality reads were removed from the raw data. Clean data of high quality were used for the downstream analyses. The reads were aligned to the reference genome (10 mm) using the split read aligner TopHat v2.0.12 and Bowtie v2.2.3, and HTSeq v0.6.1 was used to estimate the abundances of mapped genes. Expected number of Fragments Per Kilobase of transcript sequence per Million base pairs sequenced (FPKM) of each gene was calculated based on the length of the gene and reads count and used as the evaluation index of gene expression levels. For differential expression gene (DEG) analysis, the DESeq R package (1.18.0) was used to perform routine statistics with a model based on negative binomial distribution. *P*-values <0.05 were deemed significant. Next, Gene Ontology (GO) enrichment pathway analysis of DEGs was conducted using the GOseq R package, which adjusts the gene length bias based on Wallenius hyper-distribution. GO pathways with *P*-values <0.05 defined a significant enrichment of the DEGs. Protein-protein interaction (PPI) networks of the DEGs screened out by GO enrichment were performed in the STRING database (https://string-db.org/). Further analysis was performed in Cytoscape_v3.7.2 software.

Real-time quantitative PCR

Cerebella were collected at P14, and total RNA was extracted using Trizol (Invitrogen, USA) and reverse transcribed to cDNA, according to the manufacturer's protocol. Real-time PCR for target genes was performed with a SYBR Green kit (Takara Company, Japan) and the CFX Connect^{TM} Real-time system (BioRad, USA). Primers are listed in the supplementary table. Expression of mRNA was detected via the ΔΔ cycle threshold-based algorithm relative to an internal control gene (GAPDH). Each sample was run in triplicate, and 6 mice from each group were used.

Statistical analysis

All data collection and analyses were performed randomly by experimenters blinded to the genotypes. The sample sizes are similar to those of previous publications (29-31) and listed in the figure legends. Data are represented as the means ± standard deviation (SD), and statistical analysis included the Chi squared test, unpaired *t* test, two-way ANOVA, and two-way repeated-measures ANOVA with post hoc Bonferroni multiple comparisons test were performed using SPSS 19.0 software (SPSS Inc., USA). Detailed statistical approaches and results are listed in the figure legends and supplementary tables. A *P*-value < 0.05 was defined as statistically significant. In the graphed data *, **, and *** denote *P*-values less than 0.05, 0.01 and 0.001, respectively.

Results

BTBR mice exhibited infancy-onset dystonic behavior and motor impairments

Movement disorders are widely reported in combination with autism in individuals. We found BTBR mice exhibited severe dystonic movements during tail suspension, when mice try to keep an upright body posture. The most prominent dystonic symptom was hyperflexion of one or both hyperkinetic hindlimbs during tail suspension. Hindlimb clasping or fore- and hindlimb clasping, hyperextension, and severe trunk twisting were also observed in conjunction with myodystonia (Fig.s1). The dystonia in BTBR mice onset began at postnatal day 10 (P10) (X^2=3.902, P<0.05), and nearly 100% of BTBR mice exhibited significant dystonic behavior since P14 (X^2=21.505, P<0.001). This behavior persisted to adulthood and remained stable (Fig.1 A and B). Physiological hypermyotonia was observed in WT mice between P7 and P30, but it disappeared after P30. In addition, BTBR mice also developed a weakened ability to hang from a wire grid since P21 (P<0.001) compared to the WT (Fig.1 C, F(1,258) = 343.614, P < 0.001) because of abnormal hindlimb clasping or twisting in some cases. Fine motor skill was assessed using regularly and irregularly spaced horizontal ladders at 8 weeks of age. Mice ran across the horizontal ladder in two patterns, as shown in Fig.1D. BTBR mice exhibited increased limb falls in both the regular (T_{20}=2.377， P<0.05) and irregular (T_{20}=2.812, P<0.05) patterns, which suggests a deficit in fine motor skill (Fig.1E). Interestingly, the time spent crossing the ladder was decreased in BTBR mice compared to WT controls (Pattern A: T_{20}=4.381，P<0.001; Pattern B: T_{20}=6.686，P<0.001), mainly because of the increased activity. BTBR mice were also significantly hyperactive in the open field, as indicated by the increased distance in all zones (T_{16}=2.719, P<0.05) and the central zone (T_{16}=2.504, P<0.05) (Fig.1 I, J). Motor skill learning was assessed by means of the consecutive rotarod learning test (Fig.1H). BTBR and WT mice learned the task, and the time on the rod gradually increased (WT: F(4,44) = 21.867, P < 0.001; BTBR: F(4,28) = 15.306, P < 0.001). However, learning was significantly slower in the BTBR mice (F(1,72) = 28.232, P < 0.001) (Fig. 1H). Notably, the BTBR mice showed abnormal behaviors, such as attention-deficit, when they were put on the rotarod, as shown in Fig.1G. Instead of concentrating on the motor learning, the BTBR mice explored and ignored the unstable rotating rod under their feet. It may be an important cause to the impaired learning process. In summary, BTBR mice exhibited infancy-onset dystonia accompanied by severe deficits in motor coordination and motor learning in addition to autistic behavior.

BTBR mice postnatally developed hyperplastic cerebella with increased foliation

In the adult BTBR mice, the overall structure of the cerebellum was abnormal, with an obviously larger area (T_{11}=7.727, P<0.001) and more lobules (T_{11}=6.826, P<0.001) (Fig. 2A, D). By dividing the area into three lamellas, the molecular layer (ML), granule cell layer (GCL) and white matter (WM), we found that the enlarged portion was mainly in the ML (T_{11}=4.383, P<0.01) and GCL (T_{11}=8.880, P<0.001) (Fig.2 B). The thickness of the ML was not altered in BTBR mice (data not shown), and its increased area may have resulted from an elongated perimeter. Therefore, the enlargement of the cerebella may be due to the extension of the GCL. Another noticeable change was considerably more foliation in BTBR cerebella than the WT controls (Fig.2 C). To determine when BTBR mice first exhibited enhanced foliation, paraffin sections of the cerebella with HE staining were observed sequentially during the first two postnatal weeks (Fig.2 F). The initial stages of cerebellar patterning, including cardinal fissure formation, were normal in BTBR mice until P3, but the average sagittal cerebellar area increased significantly (T_9=2.447, P<0.05) compared to WT controls. The average sagittal cerebellar section perimeter was elongated concomitantly (T_9=4.378, P<0.01), which indicates that the cerebellar surface area was increased. Thus, cortical expansion and increased cross-sectional area preceded supernumerary folia in BTBR mice.

BTBR mice first exhibited increased foliation at P7, with multiple lobules that were not present in controls (T_{10}=20.125, P<0.001) (Fig. 2F and G). Additionally, the midsagittal area (T_{10}=11.234, P<0.001) and perimeter (T_{10}=20.698, P<0.001) increased more noticeably. At P14, when foliation patterns are established, BTBR were larger (T_9=6.739, P<0.001) (Fig. 2H), had a longer perimeter (T_9=10.639, P<0.001) (Fig. 2I), and were considerably more foliated than controls (T_9=22.160, P<0.001) (Fig. 2F and G).

Granule cell precursor (GCP) proliferation was increased in BTBR cerebella but migration did not change

The foliation pattern divided by fissures of different lengths is a representative morphology of cerebella. The formation is orchestrated by multicellular anchoring centers in which granule cells are the initiating factors and provide the driving physical force (32). In development, GCPs in the EGL proliferate and differentiate into granule cells, then gradually mature during migration through the ML to destinations in the IGL. BrdU was used to label the newborn GCPs in the EGL of P3 cerebella (Fig.3 A, B). Co-staining of nuclei with DAPI revealed that the EGL was much thicker in BTBR cerebella compared to WT (T_9=3.218, P<0.05) (Fig.3 A_2, B_2, C). Simultaneously, the density of BrdU-positive GCPs in the EGL increased significantly (T_9=3.910, P<0.05) (Fig.3 D). The total GCPs (T_9=3.944, P<0.05) (Fig.3 E) and proportion (T_9=4.899, P<0.01) (Fig.3 F) were also increased in BTBR mice. To confirm this result, another marker, Ki67, which is actively expressed during mitosis and degrades soon after caryomitosis, was used. Consistently, the Ki67-positive GCPs in the EGL were multiplied in BTBR mice compared to WT mice (T_9=4.273, P<0.01) (Fig. G, H, I) at P3. Ki67 was further detected at P7, and it was still much greater in BTBR mice than WT mice (T_{10}=3.747, P<0.01) (Fig.4 J, K, L). These results indicate increased granule cell precursor proliferation in the BTBR cerebella postnatally up to P7.

The granule neurons originate from the GCP in the EGL, then migrate radially through the scaffold-the Bergmann processes to reach their ultimate location in the IGL and maturation (17). To confirm whether the altered proliferation of GCPs affected this process, we investigated radial migration. We observed the distribution of mature granule neurons with NeuN staining at P7, which is the middle of the migration process. Almost all the mature granule neurons were in the IGL in WT mice, with invisible ectopic neurons in the EGL or ML (Fig.4 A). The results were similar in the BTBR, and no ectopic mature neurons were found (Fig.4 B). Notably, the EGL thickness was comparable in the two groups (T_{10}=0.856, P=0.412) (Fig.4 C), which indicates that the overproduced granule neurons in BTBR mice were transferred efficiently. It was further confirmed that migrating granule neurons identified by slim nuclei in the ML (33) were increased in BTBR mice (T_{10}=5.716, P<0.01) (Fig.s2 E), but the proportion or migrating rate was comparable between groups (T_{10}=0.679, P=0.073) (Fig.s2 F). Bergmann glia play a vital role in granule neuron migration. Therefore, we also investigated this unique cell. Bergmann glia soma and fibers were clearly stained with s100b and GFAP in each group (Fig.4 E-H). No aberrations in Bergmann glia were found between groups, neither soma (T_{10}=0.303, P=0.768) (Fig.4 I) nor fibers (T_{10}=0.770, P=0.459) (Fig.4 J). The Bergmann glia in the WT and BTBR mice had the same morphology, with soma located in the Purkinje cell layer, diffuse distribution, and 3-4 cells surrounding a Purkinje neuron. Each soma extended approximately 1-3 processes upward, across the molecular layer, and ended at the pial surface. Furthermore, Nissl staining of adult 3-month cerebella for mature neurons revealed conspicuous gross morphological changes in BTBR mice, but the neuron density was similar in the ML between groups. The boundary of the IGL was well-defined with no stranded cells, which indicates that the migration of granule neurons was accomplished, in terms of results.

Purkinje neurons in BTBR cerebella was hypotrophy with abnormal dendritic spine formation

Purkinje cells are the sole efferent neurons in the cerebella and play a key role in motor function, the development of which is regulated by multiple factors and cells. We investigated whether the Purkinje neurons of BTBR mice were affected during the critical time when the dystonia behavior reached the fastigium at P14. The Purkinje neurons were labeled with the specific marker calbindin (CB) (Fig.5 A-D). The distribution of Purkinje neurons and the development process were not different between WT and BTBR mice. Purkinje neurons were arranged in a monolayer, and the bushy dendrites grew into the ML. Purkinje neuron density was comparable in each lobe between groups (Fig.5 E) However, Purkinje neurons in BTBR cerebella exhibited significant cell soma hypotrophy compared to WT, especially the posterolateral lobes, from lobe IV to X (lobe IV/V: T_{10}=3.217, P<0.01; love VI/VII: T_{10}=5.470, P<0.001; lobe VIII: T_{10}=4.142, P<0.01; lobe IX: T_{10}=2.972, P<0.05; lobe X: T_{10}=2.649, P<0.05) (Fig.5 F). Western blotting was used to confirm this result (Fig.5 G), and calbindin protein expression was decreased in BTBR cerebella (T_{10}=2.416, P<0.05) (Fig.5 H), in accordance with the decrease in soma size. The cerebellar lobular development occurs from posterior to anterior, and lobes IX and X originally develop. Therefore, we speculated this that phenotype in BTBR was progressing. We observed the Purkinje cells in adulthood and found a sparse cell distribution with significant cell loss in the posterior lobes in BTBR mice,

including lobes VIII (T_6=3.019, P<0.05), IX (T_6=4.971, P<0.001) and X (T_6=2.662, P<0.05) (Fig.s3). These results indicate that the hypotrophy in Purkinje neurons may be a foreboding of cell death.

We investigated synaptic formation of the Purkinje dendrites. Golgi staining was used to examine the dendrites (Fig.6 A-B). Representative images showed no differences in gross morphology of Purkinje neurons between groups. There were no abnormalities in extended areas of dendrites (T_6=2.315, P=0.060) (Fig.6 C), primary dendrite length (T_6=0.951, P=0.378) (Fig.6 D), or the complexity of the dendrite arborization as assessed by Sholl analysis (F(1,204) = 0.105, P =0.757) (Fig.6 E, F) of BTBR mice. Finally, the synaptic structure was detected. Spine density in BTBR cerebella was significantly increased (T_6=5.793, P<0.01) compared to WT, with a close array in dendritic branches (Fig.6 A_1'-B_2' and H). Spines exhibited a transformed morphology during their development and maturation, which reflects different synaptic function at different stages (34). After dividing the spines into three subtypes, thin, stubby and mushroom (Fig.6 G), the maturation of the spines was generally assessed. The proportion of the immature long, thin subtype was significantly increased (T_6=6.147, P<0.01) in BTBR mice compared to WT mice, and the transitional stubby subtype (T_6=2.617, P<0.05) and mature wide-headed mushroom spines (T_6=7.738, P<0.001) were decreased (Fig.6 A_1'-B_2' and I). These results demonstrate that the formation of the spines was strongly promoted but the maturation was suffocated by some factor in BTBR mice.

Dysregulated *TRPC* genes impaired cerebellar development in BTBR mice

To examine the underlying mechanism of the abnormal cerebellar development and connection formation in BTBR mice, we performed RNA-Seq in whole cerebella tissue of WT and BTBR mice at postnatal day 14. Previous studies were performed in other brain regions of BTBR mice vs WT mice (35-37), but few studies were done in cerebella. We identified 3992 differentially expressed genes (P<0.05), with 1858 upregulated and 2134 downregulated (Fig.6 A) genes in BTBR mice compared to the WT. For functional annotation, the GO term enrichment in biological processes of differentially expressed genes was analyzed. The greatest differences primarily were involved in central nervous system development, neurogenesis, differentiation, cell development and morphogenesis (Fig.6 B), which are highly consistent with the abnormal development of the cerebella in BTBR mice. The negative regulation of nervous system development was noticeable, in the top and the coverage of cerebellar development. After further screening using protein-protein interaction (PPI) networks analysis (Fig.s4), the critical genes were identified, and significantly increased *TRPC6* was a highly suspicious candidate in BTBR mice (Fig.6 C). *TRPC6* is especially expressed during cerebellar development (38), and it regulates neurogenesis and synaptic formation (39, 40). PPI networks of the DEGs in this pathway (Fig.s4) indicated the direct interaction of *TRPC6* to the changed allele, *Itpr3*, of BTBR mice, which further supports its core status. The expression was verified using RT-PCR (Fig.6 D). We unexpectedly detected *CAMK IV* gene expression, which acts downstream of *TRPC6*, and found that it was upregulated as expected (Fig.6 E). *TRPC3* and *4* were also detected and exhibited decreased and increased expression, respectively, consistent with the RNA-seq results (Fig.6 E). Therefore, the RNA-seq suggests that *TRPC* protein, with *TRPC6* as the core

factor, mistakenly regulated the development of the cerebellum and resulted in more serious disorders over time.

Discussion

We demonstrated that BTBR mice also exhibited severe infancy-onset dystonic behaviors with significant impairments in motor coordination and motor learning, which were similar to those observed in patients with ASD. These motor dysfunctions were highly linked to the abnormal development of the cerebellum. The emerging of dystonia in BTBR mice coincided with an increasing proliferation of granule cell precursors (GCPs), which gave rise to enlargement of the inner granule layer in cerebella and enhanced foliation. Some studies indicated abnormalities in cell quantity or morphology of Purkinje neurons of autism individuals. Consistently, Purkinje neurons in BTBR mice were hypotrophic with increased dendritic spine formation but suppressed maturation. Transient receptor potential canonical channel 6 (TRPC6) was suggested to be responsible for the impaired neurodevelopment and further movement dysfunction. Our observations demonstrated that incorrect cerebellar neurogenesis occurred during the pathological progression of the comorbidities of ASD and movement disorders, and the key roles played by the TRPC protein family was worthy of attention for further study and future approaches to therapy.

Motor dysfunction represents a heterogeneous array of nondiagnostic symptoms in ASD. In this study, we identified dystonia symptoms, such as hyperflexion, clasping and twisting, elicited by tail suspension in BTBR mice. The abnormal hindlimb clasping or twisting in BTBR mice also caused a weakened ability to hang from a wire grid. Additionally, impaired fine motor skills in ASD patients are highly linked with social symptomatology (41). In agreement with these findings, we report here that BTBR mice exhibited skilled walking pattern deficits using the regularly and irregularly spaced horizontal ladder test. The rotarod task is often regarded as a test of cerebellar coordination and motor ability. WT mice showed better performance on the rotarod task across the consecutive learning test, and BTBR mice exhibited slower learning which might due to an attention deficit.

Postmortem and brain imaging studies widely identified the cerebellum as one of the most abnormal brain regions associated with motor deficits in ASD patients (19, 42). The abnormal behavior onset in BTBR mice coincided with the critical period of cerebellar development, which suggests abnormalities in the cerebellum as the neural substrate of motor impairments. Haijie Yang reported an increase in cerebellar foliation and larger gross brain volume of BTBR mice (43). In agreement with this finding, we report that increased cerebellar size and IGL area were obvious compared to the WT mice, with microscopic enhanced foliation. The phenotype was interesting because folia in the cerebellum are critical for circuit formation, which serve as a broad platform to connect afferent and efferent projections (32). Welker suggested it as the fundamental unit of sensorimotor integration (44), and disturbed foliation was involved in defects of motor coordination (45, 46). Inward accumulation of proliferated GCPs is a pivotal driving force in the cerebellar foliation, and the existing mouse model of disturbed foliation demonstrated an aberrant proliferation of GCPs (47, 48). The present study detected increased GCP proliferation and IGL expansion in the BTBR mouse cerebellum. Impaired radial migration was also

observed in rodents with increased foliation (49, 50), and a dramatic increase in foliation was credited with a prolonged period of migration of GCPs in human cerebella (51). Bergmann glia-guided migration was not altered in BTBR mice from early postnatal days to adulthood. Thus, the expansion of the cerebellar extra lobes likely arose from GCP overproliferation in BTBR mice.

Other reports suggest that PCs also participate in cerebellar foliation (32, 52). PCs anchor the outline of the cortex via axonal projections to the underlying white matter at positions that define the base of the fissures. BTBR mouse cerebellum exhibited hypotrophic Purkinje neurons at an early developmental period. The abnormal development of granule cells could ultimately regulate the growth of PCs (53–55), and we inferred that the disrupted patterning of Purkinje cells may be secondary to abnormal GC development. We cannot ignore the fact that PCs are the sole efferent neurons in cerebellum that connect to the outer brain and participate in more complicated neural activity. Abnormal PC development determined the dysfunction of cerebella. Parallel fibers extended by granule neurons in the EGL traveled up and stretched to both sides parallel to the pial surface in the ML to connect the Purkinje dendrite. Considering the multiplying granule neurons and invariable even decrease in PCs, a superabundant incoming of information to an individual PC was predictable. Moreover, the synaptic structure identified by dendritic spines in Purkinje neurons was significantly affected because many more spines existed in a lower mature proportion. Synapses were likely overproduced, but the maturation was suppressed. Immature spines likely aid in the initiation of synaptic contact (56), and mature spines contain an abundance of neurotransmitter receptors to truly support synaptic activity (34, 57). Abnormal spine formation and maturation would impact the neural circuit and disturb the allomeric function of the brain. Additionally, increasing signal income would inevitably break the physiological balance in transduction, which indicates the critical role played by disturbed information transfer in cerebellar dysfunction.

TRPC is a nonselective cation channel that dominantly modulates the Ca^{2+} entry pathway and the release of intracellular Ca^{2+} (58). TRPC3, 4 and 6 belong to the TRPC protein family and are particularly expressed in cerebella during the first 6 weeks after birth, at the critical neurogenesis period of the cerebellum, to regulate cerebellar development (38). TRPC6 plays an essential role in G2/M phase transition (59), and inhibition or activation of TRPC6 expression suppresses or accelerates cell growth (59, 60), respectively. Moreover, TRPC6 participates in the development of dendritic spines and regulates the formation of excitatory synapses in the hippocampus (40), and inhibition of TRPC6 reduces dendritic arborization and spine density (61). The results of RNA sequence analysis indicated that TRPC6 was an important regulator involved in the abnormality of cerebellar development of BTBR mice. Moreover, other autistic researches remind the relationship between TRPC6 and ASD. Wei Li found that TRPC signaling was impaired in hippocampal neurons of Mecp2 mutant mice, another ASD mouse model, which led to activity-dependent BDNF release disturbances that further accounted for sensory and motor abnormalities (62). Later, Griesi-Oliveira K demonstrated a reduction or haploinsufficiency of the TRPC6 gene in ASD individuals, which led to impaired neuronal development, morphology, and function (63). These findings suggest TRPC6 as a novel predisposing gene for ASD to elucidate autism pathophysiology.

Conclusion

We demonstrated that abnormal neurogenesis of cerebella in BTBR mice primarily affected foliation and disturbed synaptic formation, which led to dystonia-like behavior and motor dysfunction. The TRPC family, especially TRPC6, was highly indicated as responsible for the impaired cerebellar development and as a novel predisposing gene for ASD. Therefore, TRPC6 should receive more attention and be further explored to elucidate the pathological process of ASD and possible novel treatments.

Declarations

Acknowledgements

We thank Prof. Haiwei Xu for his good suggestion and excellent technical assistance.

Funding

This work was financially supported by National Natural Science Foundation of China, project #: 31871043.

Ethics approval

All of the animal breed and experiments are performed accordance with the standard guidelines of Animal Experiment Committee of Laboratory Animal Center of Army Medical University.

Authors' contribution

RX carried out the experiments, collected and analyzed data and wrote the paper. HYZ, RYZ, LW and ZLZ maintained the mice and collected the samples. XL and YYM contributed to the quantification and data analysis. XTF provided resources and funding, performed the experiments planning, supervised the project and revised the manuscript.

Competing interests

All authors read and approved the final manuscript and declared no potential conflicts of interest.

Consent for publication

Not applicable.

Availability of data and material

All the data of the current study are available from the corresponding author on reasonable request, to any qualified researchers.

Abbreviations

ADHD: Attention-deficit/hyperactivity disorder; ASD: Autism spectrum disorders; BrdU:5-bromo-2'-deoxyuridine; CB: calbindin; DAPI: 4’,6-diamidino-2-phenylindole; DCN: Deep cerebellar nuclei; DEG: Differential expression gene; EGL: External granule layer; FPKM: Fragments per kilobase of transcript sequence per millions base pairs sequenced; GCL: Granule cell layer; GCP: Granule cell precursor; GFAP: Glial fibrillary acidic protein; GO: Gene ontology; HE: Hematoxylin-eosin; IGL: Inner granule layer; *Itpr3*: Inositol triphosphate receptor 3; ML: Molecular layer; NeuN: Neuronal nuclei; P10: Postnatal day 10; PBS: Phosphate buffered saline; PC: Purkinje cell; PCL: Purkinje cell layer; PFA: Paraformaldehyde; PPI: Protein-protein interaction; RT: Room temperature; SD: Standard deviation; TBS: Tris buffered saline; *TRPC*: Transient Receptor potential canonical channel; WM: White matter; WT: Wild type.

References

1. Lord C, Elsabbagh M, Baird G, Veenstra-Vanderweele J. Autism spectrum disorder. Lancet (London, England). 2018;392(10146):508-20.
2. Constantino JN, Charman T. Diagnosis of autism spectrum disorder: reconciling the syndrome, its diverse origins, and variation in expression. The Lancet Neurology. 2016;15(3):279-91.
3. Ecker C, Bookheimer SY, Murphy DG. Neuroimaging in autism spectrum disorder: brain structure and function across the lifespan. The Lancet Neurology. 2015;14(11):1121-34.
4. Richards C, Jones C, Groves L, Moss J, Oliver C. Prevalence of autism spectrum disorder phenomenology in genetic disorders: a systematic review and meta-analysis. The lancet Psychiatry. 2015;2(10):909-16.
5. Cook J. From movement kinematics to social cognition: the case of autism. Philosophical transactions of the Royal Society of London Series B, Biological sciences. 2016;371(1693).
6. Bell L, Wittkowski A, Hare DJ. Movement Disorders and Syndromic Autism: A Systematic Review. Journal of autism and developmental disorders. 2019;49(1):54-67.
7. Robledo J, Donnellan AM, Strandt-Conroy K. An exploration of sensory and movement differences from the perspective of individuals with autism. Frontiers in integrative neuroscience. 2012;6:107.
8. Uljarevic M, Hedley D, Alvares GA, Varcin KJ, Whitehouse AJO. Relationship between early motor milestones and severity of restricted and repetitive behaviors in children and adolescents with autism spectrum disorder. Autism research : official journal of the International Society for Autism Research. 2017;10(6):1163-8.
9. Baranek GT, Woynaroski TG, Nowell S, Turner-Brown L, DuBay M, Crais ER, et al. Cascading effects of attention disengagement and sensory seeking on social symptoms in a community sample of infants at-risk for a future diagnosis of autism spectrum disorder. Developmental cognitive neuroscience. 2018;29:30-40.
10. Hara Y, Ago Y, Taruta A, Katashiba K, Hasebe S, Takano E, et al. Improvement by methylphenidate and atomoxetine of social interaction deficits and recognition memory impairment in a mouse model of valproic acid-induced autism. Autism research : official journal of the International Society for Autism Research. 2016;9(9):926-39.

11. Amaral DG, Schumann CM, Nordahl CW. Neuroanatomy of autism. Trends in neurosciences. 2008;31(3):137-45.
12. Blatt GJ. The neuropathology of autism. Scientifica. 2012;2012:703675.
13. Wegiel J, Flory M, Kuchna I, Nowicki K, Ma SY, Imaki H, et al. Stereological study of the neuronal number and volume of 38 brain subdivisions of subjects diagnosed with autism reveals significant alterations restricted to the striatum, amygdala and cerebellum. Acta neuropathologica communications. 2014;2:141.
14. Wegiel J, Kuchna I, Nowicki K, Imaki H, Wegiel J, Marchi E, et al. The neuropathology of autism: defects of neurogenesis and neuronal migration, and dysplastic changes. Acta neuropathologica. 2010;119(6):755-70.
15. Jaber M. [The cerebellum as a major player in motor disturbances related to Autistic Syndrome Disorders]. L'Encephale. 2017;43(2):170-5.
16. Menashe I, Grange P, Larsen EC, Banerjee-Basu S, Mitra PP. Co-expression profiling of autism genes in the mouse brain. PLoS computational biology. 2013;9(7):e1003128.
17. Xu H, Yang Y, Tang X, Zhao M, Liang F, Xu P, et al. Bergmann glia function in granule cell migration during cerebellum development. Mol Neurobiol. 2013;47(2):833-44.
18. Altman J, Bayer SA. Prenatal development of the cerebellar system in the rat. I. Cytogenesis and histogenesis of the deep nuclei and the cortex of the cerebellum. The Journal of comparative neurology. 1978;179(1):23-48.
19. Hampson DR, Blatt GJ. Autism spectrum disorders and neuropathology of the cerebellum. Front Neurosci. 2015;9:420.
20. Martinez S, Andreu A, Mecklenburg N, Echevarria D. Cellular and molecular basis of cerebellar development. Front Neuroanat. 2013;7:18.
21. Fatemi SH, Aldinger KA, Ashwood P, Bauman ML, Blaha CD, Blatt GJ, et al. Consensus paper: pathological role of the cerebellum in autism. Cerebellum. 2012;11(3):777-807.
22. Liu YB, Tewari A, Salameh J, Arystarkhova E, Hampton TG, Brashear A, et al. A dystonia-like movement disorder with brain and spinal neuronal defects is caused by mutation of the mouse laminin beta1 subunit, Lamb1. eLife. 2015;4.
23. Pappas SS, Darr K, Holley SM, Cepeda C, Mabrouk OS, Wong JM, et al. Forebrain deletion of the dystonia protein torsinA causes dystonic-like movements and loss of striatal cholinergic neurons. eLife. 2015;4:e08352.
24. Metz GA, Whishaw IQ. Cortical and subcortical lesions impair skilled walking in the ladder rung walking test: a new task to evaluate fore- and hindlimb stepping, placing, and co-ordination. Journal of neuroscience methods. 2002;115(2):169-79.
25. Cai Y, Wang L, Xiao R, Li X, He X, Gao J, et al. Autism-like behavior in the BTBR mouse model of autism is improved by propofol. Neuropharmacology. 2017;118:175-87.

26. Xiao R, Yu D, Li X, Huang J, Jing S, Bao X, et al. Propofol Exposure in Early Life Induced Developmental Impairments in the Mouse Cerebellum. Front Cell Neurosci. 2017;11:373.
27. Piochon C, Kloth AD, Grasselli G, Titley HK, Nakayama H, Hashimoto K, et al. Cerebellar plasticity and motor learning deficits in a copy-number variation mouse model of autism. Nature communications. 2014;5:5586.
28. Risher WC, Ustunkaya T, Singh Alvarado J, Eroglu C. Rapid Golgi analysis method for efficient and unbiased classification of dendritic spines. PLoS One. 2014;9(9):e107591.
29. Huang J, Jing S, Chen X, Bao X, Du Z, Li H, et al. Propofol Administration During Early Postnatal Life Suppresses Hippocampal Neurogenesis. Molecular neurobiology. 2016;53(2):1031-44.
30. Huang T-N, Yen T-L, Qiu LR, Chuang H-C, Lerch JP, Hsueh Y-P. Haploinsufficiency of autism causative gene impairs olfactory discrimination and neuronal activation of the olfactory system in mice. Molecular autism. 2019;10:5.
31. Xie W, Ge X, Li L, Yao A, Wang X, Li M, et al. Resveratrol ameliorates prenatal progestin exposure-induced autism-like behavior through ERβ activation. Molecular autism. 2018;9:43.
32. Sudarov A, Joyner AL. Cerebellum morphogenesis: the foliation pattern is orchestrated by multi-cellular anchoring centers. Neural Dev. 2007;2:26.
33. Yang Y, Tang Y, Xing Y, Zhao M, Bao X, Sun D, et al. Activation of Liver X Receptor Is Protective Against Ethanol-Induced Developmental Impairment of Bergmann Glia and Purkinje Neurons in the Mouse Cerebellum. Molecular Neurobiology. 2013;49(1):176-86.
34. Nimchinsky EA, Sabatini BL, Svoboda K. Structure and function of dendritic spines. Annu Rev Physiol. 2002;64:313-53.
35. Kratsman N, Getselter D, Elliott E. Sodium butyrate attenuates social behavior deficits and modifies the transcription of inhibitory/excitatory genes in the frontal cortex of an autism model. Neuropharmacology. 2016;102:136-45.
36. Mychasiuk R, Rho JM. Genetic modifications associated with ketogenic diet treatment in the BTBR mouse model of autism spectrum disorder. Autism research : official journal of the International Society for Autism Research. 2017;10(3):456-71.
37. Provenzano G, Corradi Z, Monsorno K, Fedrizzi T, Ricceri L, Scattoni ML, et al. Comparative Gene Expression Analysis of Two Mouse Models of Autism: Transcriptome Profiling of the BTBR and En2 (-/-) Hippocampus. Front Neurosci. 2016;10:396.
38. Huang WC, Young JS, Glitsch MD. Changes in TRPC channel expression during postnatal development of cerebellar neurons. Cell calcium. 2007;42(1):1-10.
39. Xu P, Xu J, Li Z, Yang Z. Expression of TRPC6 in renal cortex and hippocampus of mouse during postnatal development. PLoS One. 2012;7(6):e38503.
40. Zhou J, Du W, Zhou K, Tai Y, Yao H, Jia Y, et al. Critical role of TRPC6 channels in the formation of excitatory synapses. Nature neuroscience. 2008;11(7):741-3.

41. LeBarton ES, Iverson JM. Fine motor skill predicts expressive language in infant siblings of children with autism. Dev Sci. 2013;16(6):815-27.
42. Wang SS, Kloth AD, Badura A. The cerebellum, sensitive periods, and autism. Neuron. 2014;83(3):518-32.
43. Yang H, Huh SO, Hong JS. Enhancement of Short-Term Memory by Methyl-6-(Phenylethynyl)-Pyridine in the BTBR T+tf/J Mouse Model of Autism Spectrum Disorder. Endocrinology and metabolism (Seoul, Korea). 2015;30(1):98-104.
44. Welker WI. The significance of foliation and fissuration of cerebellar cortex. The cerebellar folium as a fundamental unit of sensorimotor integration. Archives italiennes de biologie. 1990;128(2-4):87-109.
45. Chen YT, Collins LL, Uno H, Chang C. Deficits in motor coordination with aberrant cerebellar development in mice lacking testicular orphan nuclear receptor 4. Molecular and cellular biology. 2005;25(7):2722-32.
46. Le Roy-Duflos I. Possible causal relationships between cerebellar patterns of foliation and hindlimb coordination in laboratory mice: a quantitative trait locus analysis. Behavior genetics. 2001;31(1):29-37.
47. Corrales JD, Blaess S, Mahoney EM, Joyner AL. The level of sonic hedgehog signaling regulates the complexity of cerebellar foliation. Development. 2006;133(9):1811-21.
48. Wefers AK, Lindner S, Schulte JH, Schüller U. Overexpression of Lin28b in Neural Stem Cells is Insufficient for Brain Tumor Formation, but Induces Pathological Lobulation of the Developing Cerebellum. Cerebellum. 2017;16(1):122-31.
49. Hosaka YZ, Neki Y, Hasebe M, Shinozaki A, Uehara M. Formation of excess sublobules in the cerebellum of hypothyroid rats. Annals of anatomy = Anatomischer Anzeiger : official organ of the Anatomische Gesellschaft. 2012;194(4):329-33.
50. Ryan KE, Kim PS, Fleming JT, Brignola E, Cheng FY, Litingtung Y, et al. Lkb1 regulates granule cell migration and cortical folding of the cerebellar cortex. Dev Biol. 2017;432(1):165-77.
51. Sillitoe RV, Joyner AL. Morphology, molecular codes, and circuitry produce the three-dimensional complexity of the cerebellum. Annual review of cell and developmental biology. 2007;23:549-77.
52. Altman J BS. Development of the Cerebellar System in Relation to its Evolution, Structure, and Functions. New York: CRC Press. 1997.
53. Sadakata T, Mizoguchi A, Sato Y, Katoh-Semba R, Fukuda M, Mikoshiba K, et al. The secretory granule-associated protein CAPS2 regulates neurotrophin release and cell survival. The Journal of neuroscience : the official journal of the Society for Neuroscience. 2004;24(1):43-52.
54. Salinas PC, Fletcher C, Copeland NG, Jenkins NA, Nusse R. Maintenance of Wnt-3 expression in Purkinje cells of the mouse cerebellum depends on interactions with granule cells. Development. 1994;120(5):1277-86.
55. Shimada A, Mason CA, Morrison ME. TrkB signaling modulates spine density and morphology independent of dendrite structure in cultured neonatal Purkinje cells. J Neurosci. 1998;18(21):8559-

70.
56. Dunaevsky A, Tashiro A, Majewska A, Mason C, Yuste R. Developmental regulation of spine motility in the mammalian central nervous system. Proceedings of the National Academy of Sciences of the United States of America. 1999;96(23):13438-43.
57. Matsuzaki M, Ellis-Davies GC, Nemoto T, Miyashita Y, Iino M, Kasai H. Dendritic spine geometry is critical for AMPA receptor expression in hippocampal CA1 pyramidal neurons. Nat Neurosci. 2001;4(11):1086-92.
58. Dietrich A, Gudermann T. TRPC6. Handbook of experimental pharmacology. 2007(179):125-41.
59. Shi Y, Ding X, He ZH, Zhou KC, Wang Q, Wang YZ. Critical role of TRPC6 channels in G2 phase transition and the development of human oesophageal cancer. Gut. 2009;58(11):1443-50.
60. Cai R, Ding X, Zhou K, Shi Y, Ge R, Ren G, et al. Blockade of TRPC6 channels induced G2/M phase arrest and suppressed growth in human gastric cancer cells. International journal of cancer. 2009;125(10):2281-7.
61. Tai Y, Feng S, Ge R, Du W, Zhang X, He Z, et al. TRPC6 channels promote dendritic growth via the CaMKIV-CREB pathway. Journal of cell science. 2008;121(Pt 14):2301-7.
62. Li W, Calfa G, Larimore J, Pozzo-Miller L. Activity-dependent BDNF release and TRPC signaling is impaired in hippocampal neurons of Mecp2 mutant mice. Proceedings of the National Academy of Sciences of the United States of America. 2012;109(42):17087-92.
63. Griesi-Oliveira K, Acab A, Gupta AR, Sunaga DY, Chailangkarn T, Nicol X, et al. Modeling non-syndromic autism and the impact of TRPC6 disruption in human neurons. Molecular psychiatry. 2015;20(11):1350-65.

Figures

Figure 1

BTBR mice exhibited infancy-onset dystonic behavior and motor impairments. A Representative image of BTBR mice and WT control at each growing point in tail-suspension test. B Quantification of the morbidity of dystonia showing BTBR mice developed typical dystonic behavior and aggravated with growth. (Chi square test; n=32, 26 mice) C Latency to fall from the wire grid, and BTBR mice developed a weaken ability to hang since adolescence. (Two-way ANOVA; n=15-29 mice) D The horizontal ladder rung walking apparatus with regular arrangement (pattern A) and irregular arrangement (pattern B). E Average total number of limbs fall in the horizontal ladder rung walking task. (Student's t-test; n=10, 12 mice) F Quantification of the time to across the horizontal ladder. (Student's t-test; n=10, 12 mice) G Representative images in the rotarod test showing attention deficit in BTBR mice. H Latency to fall from the accelerated rod showing motor and motor learning defect in BTBR mice. (Two-way repeated measure test; n=12, 8 mice) I Representative trace diagrams in open field test showing hyperactivity in BTBR mice.

J Quantification of the distance in total and central area of the open field. (Student's t-test; n=9, 9 mice) All data are displayed as mean ± SD. *P < 0.05, **P < 0.01, ***P < 0.001.

Figure 2

Cerebellar cortex in BTBR mice was expanded with increased foliation since post-natal. A DAPI stained cerebella of WT and BTBR mice at adult stage (P90). B Quantification of the sagittal area of cerebella and each component at adulthood. (Student's t-test; n=6,7 mice) C Quantification of the average lobe number showing increased foliation of adult BTBR mice. (Student's t-test; n=6,7 mice) D Whole mount images and sagittal section of brain in WT and BTBR mice at adult stage (P90). White and black dotted line delimit the lobule outline. Black arrowheads indicate the lobule fissures. E Schema graph illustrating the determination of perimeter and area. F Hematoxylin-eosin (HE) staining of middle sagittal cerebellar section at postnatal day 3, 7 and 14 (additional lobes highlighted in red in the counterdraw). G Quantification of the average lobule number in WT and BTBR mice at indicated stage. (Student's t-test; P3 n=6,5; P7 n=6,6; P14 n=5,6) H Quantification of the average sagittal cerebellar area in WT and BTBR mice at indicated stage. (Student's t-test; P3 n=6,5; P7 n=6,6; P14 n=5,6) I Quantification of the average sagittal cerebellar section perimeter in WT and BTBR mice at indicated stage. (Student's t-test; P3 n=6,5; P7 n=6,6; P14 n=5,6) All data are displayed as mean ± SD. *P < 0.05, **P < 0.01, ***P < 0.001. Scale bar: A, F 200μm; D 1mm.

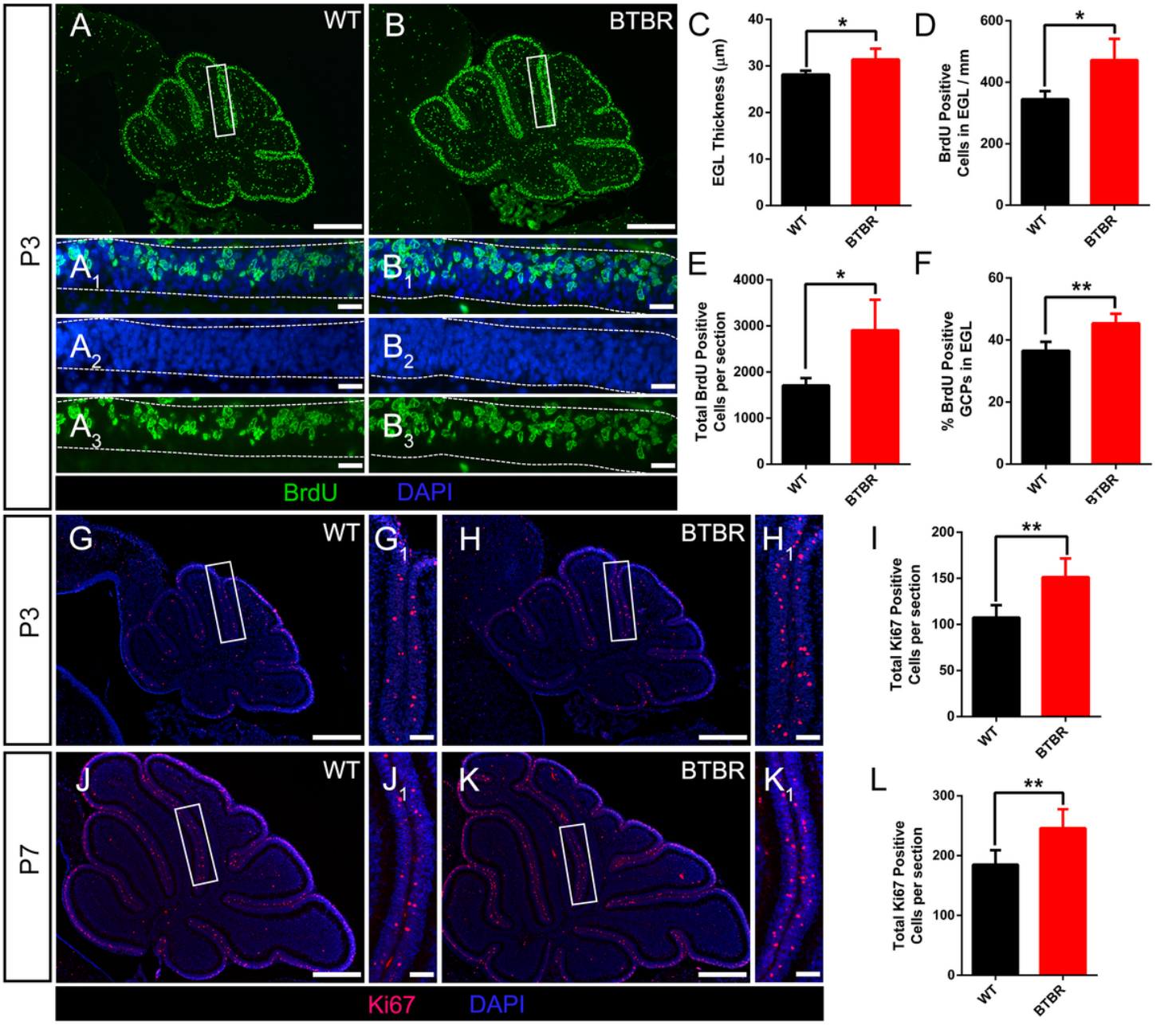

Figure 3

Granule cell precursor proliferation was increased in BTBR mice postnatally. A-B BrdU staining (green) of sagittal section of cerebellar vermis at P3. Dotted line in A1-A3 and B1-B3 delimit external granular layer (EGL) where proliferative granule cells originate. Nucleus was counterstained with DAPI (blue). C Quantification of the EGL thickness showing thicker EGL in BTBR mice at P3. (Student's t-test; n=6,5) D Quantification of BrdU positive cells in EGL per mm in each group at P3. (Student's t-test; n=6,5) E Quantification of total BrdU positive cells in EGL of sagittal section at P3. (Student's t-test; n=6,5) F Quantification of the percentage of BrdU positive cells in EGL at P3. (Student's t-test; n=6,5) G-H Ki67 staining (red) of sagittal section of cerebellar vermis at P3. Nucleus was counterstained with DAPI (blue). White panels in G, H are magnified in G1 and H1. I Quantification of total Ki67 positive cells in EGL of sagittal section at P3. (Student's t-test; n=6,5) J-K Ki67 staining (red) of sagittal section of cerebellar

vermis at P7. Nucleus was counterstained with DAPI (blue). White panels in J, K are magnified in J1 and K1. I Quantification of total Ki67 positive cells in EGL of sagittal section at P3. (Student's t-test; n=6,6) All data are displayed as mean ± SD. *P < 0.05, **P < 0.01. Scale bar: A, B, G, H, J, K 200μm; A1-A3, B1-B3 10μm; G1, H1, J1, K1 20μm.

Figure 4

Radial migration of granule neurons in cerebella was not altered in BTBR mice. A-B NeuN stained (red) granule cells showing mature neurons were all distributed in inner granular layer (IGL) both in WT and BTBR mice at P7. Nucleus was counterstained with DAPI (blue). C Quantification of EGL thickness in each group at P7. (Student's t-test; n=6,6) D Schema graph of sagittal cerebella illustrating the observed region (black panel) in figure E-H. E-F S100b positive Bergman glia somas in Purkinje cell layer (PCL) at P7. G-H GFAP positive Bergmann glia fibers in molecular layer (ML) at P7. I Quantification of Bergman glia somas in PCL per mm. (Student's t-test; n=6,6) J Quantification of Bergman glia fibers in ML per mm. (Student's t-test; n=6,6) K-N Nissl staining of middle sagittal cerebellar section in adult (P90) WT and BTBR mice. L and N are Magnified images of black panels in K and M. Dotted line in L, N indicate the boundary between ML and PCL. All data are displayed as mean ± SD. Scale bar: A, B, K, M 200μm; E-H, L, N 10μm.

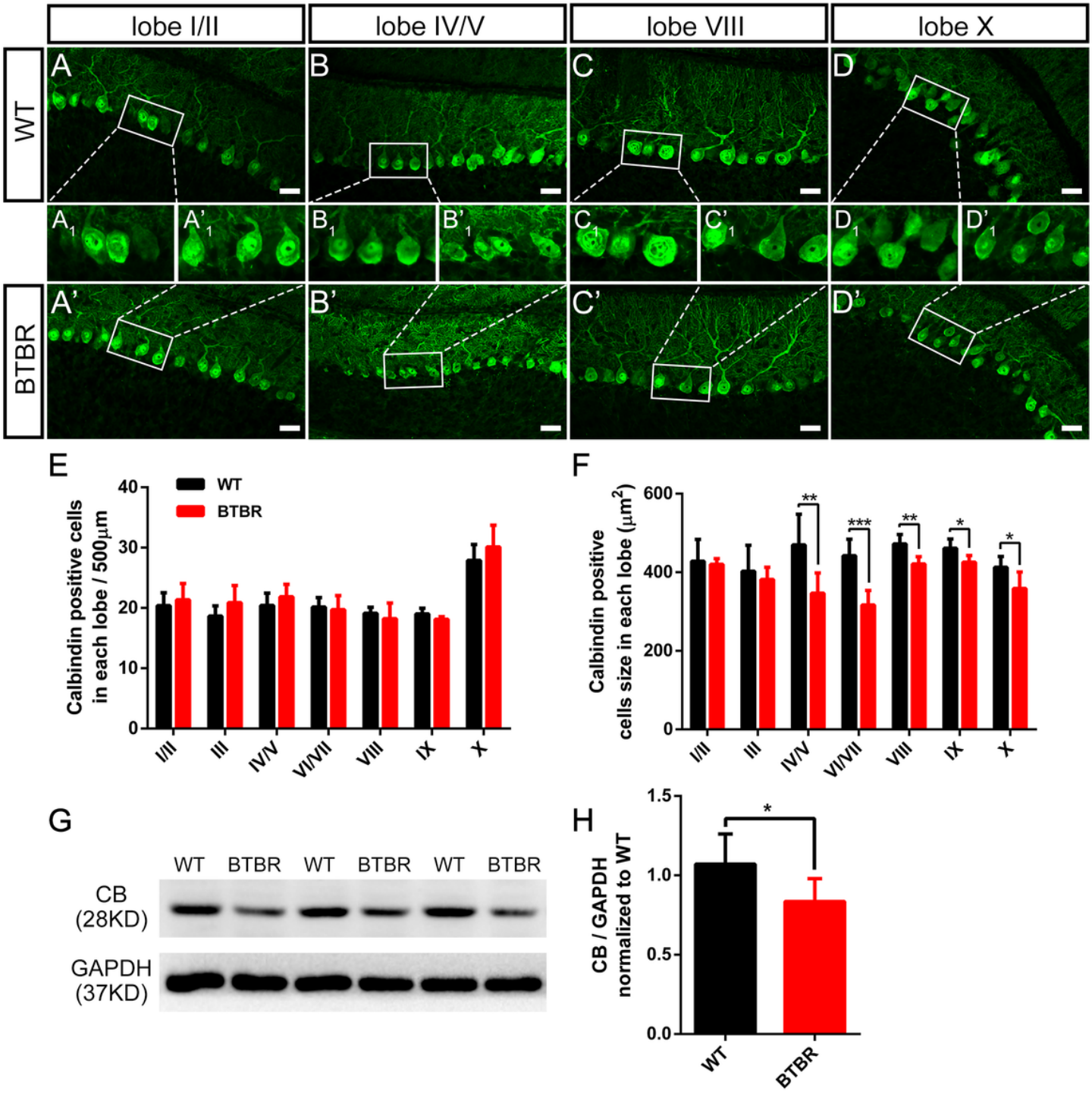

Figure 5

Purkinje neurons' density did not variate but was significantly hypotrophy in BTBR mice at postnatal day 14. A-D Calbindin staining Purkinje neurons in cerebellar lobe I/II, IV/V, VIII, X of WT (A-D) and BTBR (A'-D') mice at P14. Purkinje neuron somas in white panels are magnified in A1-D1 and A'1-D'1. E Quantification of Purkinje neurons number per 500µm in lobe I-X. (Student's t-test; n=6,6) F Quantification of Purkinje neurons soma size showing hypotrophy in lobe VI-X of BTBR mice. (Student's t-test; n=6,6) G Representative image of western blotting for calbindin protein in WT and BTBR mice at P14. H

Densitometric quantification of calbindin showing decreased expression in BTBR mice cerebella. (Student's t-test; n=6,6) All data are displayed as mean ± SD. *P < 0.05, **P < 0.01, ***P < 0.001. Scale bar: A-D 25μm.

Figure 6

Dendritic spines of Purkinje neurons in BTBR mice were significantly increased with disturbed maturation at postnatal day 14. A-B Golgi-stained Purkinje neurons in cerebella of WT and BTBR mice. Dendritic branches in white panels are magnified in A', B' and furtherly magnified in A'1, A'2, B'1, B'2 showing increased and immature dendritic spines in BTBR mice. Yellow, blue and red arrowheads indicate thin, stubby and mushroom spine types respectively. C Quantification of Purkinje neuron dendritic profile area in each group. (Student's t-test; n=4,4) D Quantification of the length of the Purkinje neuron's primary dendrite in each group. (Student's t-test; n=4,4) E Schema graph showing the method of sholl analysis. Purkinje neuron's branches are incised by concentric circles with 5.5μm radius steps from the soma. F Quantification of intersections of branches and circles at different radius showing similar level of dendrite arborization in WT and BTBR mice. (Two-way repeated measure test; n=4, 4 mice) G Schema graph illustrating the spine maturity progresses (up to down) from long thin structure (yellow) to transitional stubby (blue) and mushroom mature form (red). H Quantification of dendritic spines of Purkinje neurons per 10μm branch showing increased spine density in BTBR mice. (Student's t-test; n=4,4) I Quantification of the percentage of each spine type showing immature development trend in BTBR mice. (Student's t-test; n=4,4) All data are displayed as mean ± SD. *P < 0.05, **P < 0.01, ***P < 0.001. Scale bar: A-B 25μm; A'-B' 5μm; A'1, A'2, B'1, B'2 2μm.

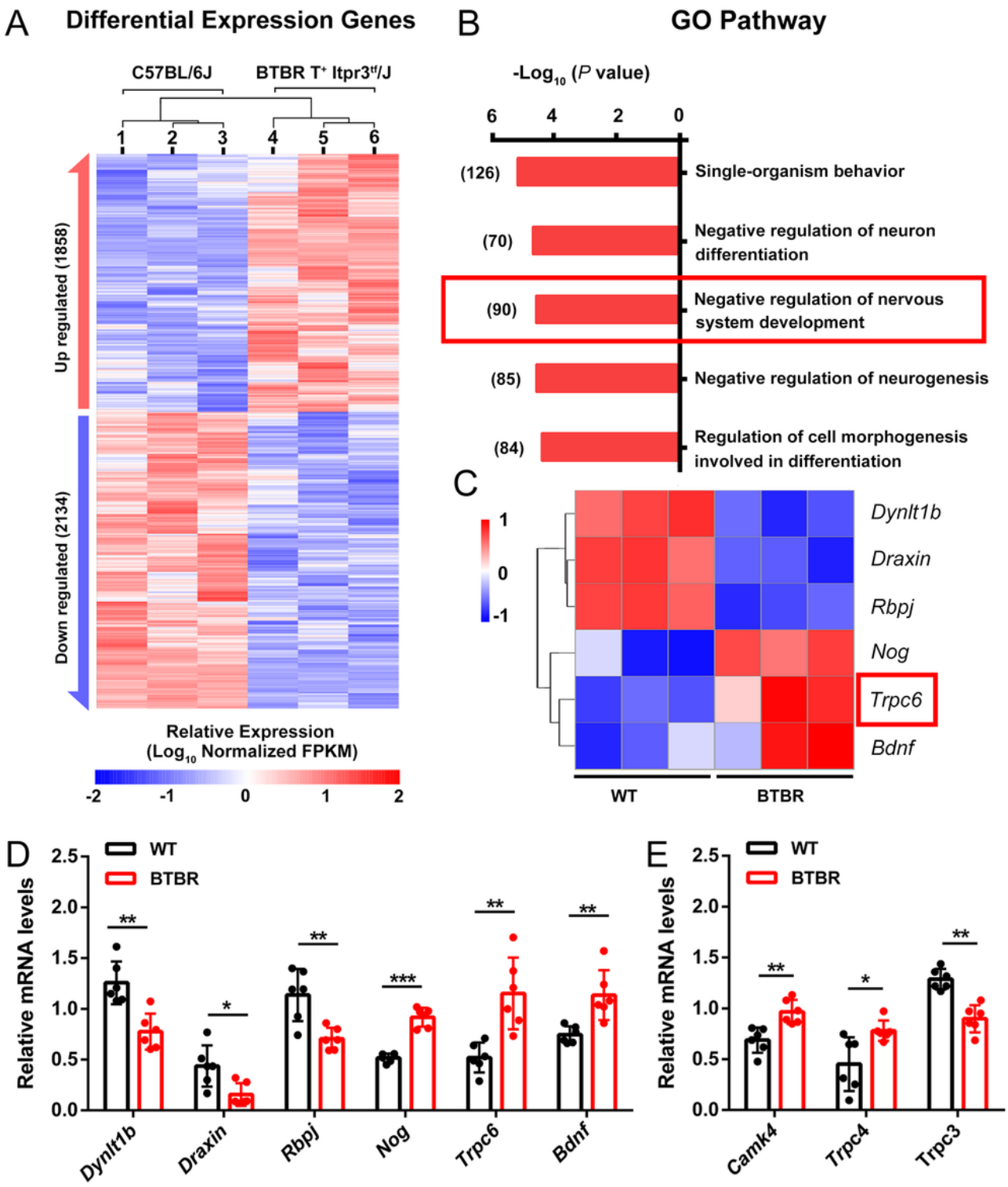

Figure 7

Trpc6 differential expression disturbed cerebellar development in BTBR mice at postnatal day 14. A Hierarchical clustering of differential expression genes in cerebella of C57BL/6J and BTBR mice at postnatal day 14. B Enriched top five GO pathway in biological process. The former significant pathway involved in cerebella development is highlighted in red frame. Number of differentially expressed genes in each pathway is list side to the bar. C Heat map depicting 6 significant genes idenfitied from highlighted

pathway in B with PPI by STRING (Fig.s2). Trpc6 is highlighted in red frame. D Validation of gene expression in control and BTBR mice by real time PCR. E Validation of Trpc3, Trcp4 and Camk4 genes expression in control and BTBR mice by real time PCR.

Supplementary Files

This is a list of supplementary files associated with this preprint. Click to download.

- Supplementallegend.docx
- SupplementalPCRprimer.docx
- stastics.xlsx